Journal of the American Ceramic Society

RESEARCH ARTICLE OPEN ACCESS

Effect of Yttrium Doping on Titanium Dioxide

Fatma Aydın Ünal[1] | Murat Ünal[2] | Sebahat Topal[3]

[1]Department of Metallurgy and Materials Engineering, Alanya Alaaddin Keykubat University, Antalya, Türkiye | [2]Department of Chemistry, Istanbul Technical University, Istanbul, Türkiye | [3]Karlsruhe Institute of Technology, Institute of Nanotechnology, Eggenstein-Leopoldshafen, Germany

Correspondence: Fatma Aydın Ünal (fatma.aydin@alanya.edu.tr)

Received: 2 March 2026 | **Revised:** 21 May 2026 | **Accepted:** 12 June 2026

Keywords: band gap narrowing | methylene blue degradation | photocatalysis | sol–gel method

ABSTRACT

The wide band gap and chemical–mechanical stability of titanium dioxide (TiO_2) make it one of the most important semiconductor materials for photocatalytic applications. However, its performance is limited by its low absorption in the visible light region. In this study, yttrium (Y)-doped TiO_2 (Y/TiO_2) powders containing 1%, 5%, and 10% Y were synthesized via the sol–gel method to improve visible-light absorption. The effects of Y doping on morphology, elemental composition, crystal structure, optical properties, and photocatalytic activity were investigated using a range of analytical techniques, including SEM/EDS, XRD, particle size analysis, and UV-Vis spectroscopy. The synthesized Y/TiO_2 samples exhibited spherical morphology, with the average particle sizes decreasing from 232 nm (pure TiO_2) to 50.24 nm (5% Y doping). Y doping significantly reduced the optical band gap of TiO_2 from 3.22 to 2.86 eV. The photocatalytic performance of the synthesized TiO_2 catalysts was evaluated via methylene blue photodegradation, and all doped samples exhibited higher activity under visible light compared to pure TiO_2. The 5% Y/TiO_2 sample demonstrated the highest photocatalytic performance, achieving up to 91% methylene blue degradation and establishing it as the optimum doping level for enhanced activity.

1 | Introduction

In recent years, various semiconductor materials, including ZnO [1], TiO_2 [2], SnO_2 [3], and Nb_2O_5 [4], have been used in solar cell applications [5, 6]. Among these, TiO_2 is the most widely used photocatalytic material. TiO_2 is an *n*-type semiconductor with low conductivity [7, 8]. As the polymorph of TiO_2, it has three phases: anatase, rutile, and brookite. Each of these phases is defined by a high refractive index, low absorption, and scattering in the visible and near-infrared spectral regions [9, 10]. Anatase TiO_2 has received more attention than the rutile and brookite phases in photocatalytic research [11, 12]. TiO_2 nanostructures are considered promising photocatalytic materials due to their remarkable photocatalytic activity, low toxicity, thermal stability, high oxidation, high efficiency, and relatively low cost when excited by ultraviolet (UV) light [13]. However, their photocatalytic performance is restricted by a wide band gap. The band gap is 3.2 eV for anatase TiO_2. It is also limited by a high rate of charge carrier recombination. The efficiency of the photocatalyst is further reduced by rapid electron–hole pair recombination [14]. Thus, the development of photocatalysts capable of activation under visible light is crucial for effectively harnessing sunlight as a primary energy source. The photocatalytic performance of TiO_2 can be improved by reducing the particle size, increasing the surface area, or sensitizing it with dye molecules or doping with metals or non-metals [15, 16]. Among these methods, rare earth (RE) metal doping is a popular technique for reducing the recombination rate of photogenerated carriers, extending the absorption wavelength to the visible region, and enhancing the photoactivity of TiO_2. RE metal doping enhances the photocatalytic performance of TiO_2 by improving contaminant adsorption, inhibiting the anatase-to-rutile phase transformation, and reducing crystallite size [17]. This increased interest in RE doping arises from the unique

electronic structure of RE ions, particularly their partially filled 4f orbitals, which facilitate interaction with functional groups. Consequently, RE doping induces oxygen vacancies, suppresses electron–hole recombination, and improves both charge separation efficiency and overall photocatalytic activity of TiO_2 [18, 19].

Many studies have reported that the concentration of RE metal dopants significantly affects photoactivity: in particular, lanthanide doped TiO_2 systems such as Sm [20], La [21], Nd [22], Dy [23], and Ce [24] have demonstrate superior improving photocatalytic performance compared to pure TiO_2, mainly due to enhanced visible-light response and improved charge separation, which results in higher photocatalytic efficiency [25]. Guan and Zhou investigated RE-doped TiO_2 synthesized via a sol–gel combined microwave hydrothermal method and reported that RE doping extends the optical absorption into the visible region while suppressing electron-hole recombination, thereby enhancing photocatalytic activity [26].

Among all RE ions, the Y^{3+} ion is considered an effective, typical dopant used to modify the electronic structure and optical properties of TiO_2. Y/TiO_2 can reduce the recombination rate of electron/hole pairs formed as a result of photogeneration, which in turn increases the photocatalytic efficiency of TiO_2 [17]. In a study by Rajput et al., Y/TiO_2 nanostructures prepared via chemical coprecipitation showed doping-dependent photocatalytic activity, with the sample containing 6% Y exhibiting the highest degradation efficiency for methylene blue (MB) under UV irradiation [27]. Similarly, Li et al. reported that Y doping enhances photocatalytic performance through synergistic effects involving Ti^{3+} species and OV, leading to improved charge separation and significantly higher degradation efficiency of Rhodamine B [28, 29]. The improvement in photocatalytic activity is mainly attributed to the role of Y doping in increasing oxygen vacancy concentration, modifying the band structure, and suppressing charge recombination [7, 17]. Additionally, the substitution of Ti^{4+} ions (0.068 nm) with larger Y^{3+} ions (0.089 nm) is structurally favorable, promoting lattice distortion and oxygen vacancy formation [30]. These effects collectively enhance light absorption and catalytic efficiency. Various synthesis methods, such as sol-gel [31], microwave [32], hydrothermal [33], microemulsion [34], chemical vapor deposition [35], c [36], solvothermal [37], solid-state [38], and sonochemical routes [39] have been employed for the preparation of Y/TiO_2. Among them, Kubiak and Cegłowski compared microwave and hydrothermal methods for Y/TiO_2 synthesis and reported that microwave-assisted samples exhibited superior photocatalytic activity in the degradation of carbamazepine [40]. The sol–gel method is of particular importance because it allows precise control over chemical reactions and material properties throughout the synthesis process [41, 42]. It is a cost-effective technique that enables the production of materials with tailored properties. In this process, a liquid precursor is first transformed into a gel and subsequently converted into a solid oxide material through drying and thermal treatment [43]. The sol–gel method is widely used for surface modification of materials and is advantageous in producing high surface area structures with stable properties. The final chemical and physical characteristics of the obtained materials strongly depend on the experimental conditions [44]. Therefore, the sol–gel method provides effective control over particle size, crystallinity, and microstructure of TiO_2-based materials [45].

In this context, considering that various studies have reported enhanced photocatalytic activity of RE-doped TiO_2 using different synthesis routes, comparative studies on Y/TiO_2 with different doping levels (1%, 5%, and 10%) prepared via the sol–gel method remain limited. Therefore, this study investigates the effect of Y doping concentration on the structural, morphological, optical, and photocatalytic properties of TiO_2. For this purpose, pure and Y/TiO_2 samples (0%, 1%, 5%, and 10%) were synthesized via the sol–gel method, and their photocatalytic performance was evaluated through MB degradation under UV irradiation. The results demonstrate that Y-doped samples exhibit higher photocatalytic efficiency compared to pure TiO_2.

2 | Methods

2.1 | Chemicals

Titanium (IV) butoxide (Sigma Aldrich), yttrium nitrate hexahydrate (Sigma Aldrich), distilled water, ethyl alcohol (Sigma Aldrich), citric acid monohydrate (Merck), acetylacetone (Sigma Aldrich), and methylene blue (Sigma Aldrich).

2.2 | Instruments

An x-ray powder diffractometer (PANalytical Empyrean XRD) equipped with CuKα radiation (λ = 0.1541 nm) was used to analyze the crystal structure and composition of TiO_2 powders over a 2θ range from 10°to 80°. The photocatalytic performance of pure and metal-doped TiO_2 samples was evaluated using a UV-Vis spectrophotometer (Hitachi U-0080D). Particle size distribution was determined by Dynamic Light Scattering (DLS) analysis (Malvern/Nano ZS90). Surface morphology, particle size, and elemental composition were further examined using a Zeiss Sigma 300 scanning electron microscope (SEM) equipped with an energy-dispersive x-ray (EDS) analyzer operating at 25 kV.

2.3 | Synthesis of Y-Doped TiO_2 Powders

First, 0.4 mL of titanium (IV) butoxide was dissolved in 10 mL of pure ethanol and stirred for approximately 40 min to form Solution A. In a separate beaker, Solution B was prepared by dissolving stoichiometric amounts of yttrium nitrate hexahydrate in 10 mL of ethanol, corresponding to doping concentrations of 1%, 5%, and 10% (0.00383 g, 0.01 mmol; 0.0195 g, 0.05 mmol; and 0.0383 g, 0.10 mmol, respectively). Solution B was then added dropwise to Solution A under continuous magnetic stirring at 500–800 rpm. Concurrently, a third solution was prepared by dissolving 0.63 g (3 mmol) of citric acid and 1 mL (9.7 mmol) of acetylacetone in 15 mL of ethanol, which was subsequently added dropwise to the mixture of A and B to yield Mixture C. The resulting mixture was continuously stirred for approximately 5.5 h until a homogeneous gel was formed. The obtained gel was dried in an oven at 90°C for 12 h. Finally, the Y/TiO_2 samples were obtained by annealing the dried gel in a furnace at 450°C for

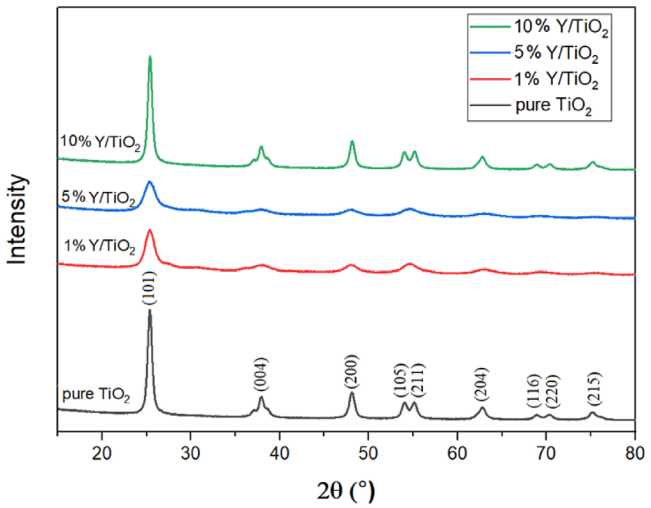

FIGURE 1 | XRD analysis pattern of synthesized TiO_2 powders.

2 h under an air atmosphere. For comparison, a pure (0%) TiO_2 sample was prepared following the same procedure [8].

3 | Results

3.1 | Structural Study

3.1.1 | X-ray Diffraction (XRD) of Pure (0%) and Y/TiO_2 Powders

To obtain detailed information about the structural properties of the synthesized TiO_2 powders, the crystallite sizes, dislocation densities, and microstrain values of the powders were calculated using the XRD pattern data. The XRD patterns of pure and Y/TiO_2 powders synthesized using the sol–gel method are shown in Figure 1. The XRD pattern confirmed the presence of the TiO_2-anatase phase and exhibited prominent diffraction peaks of anatase (in agreement with JCPDS file ICSD 00-021-1272 # 21–1272) [46, 47]. The prominent peaks of Y/TiO_2 were observed at 25.34°, 37.92°, 48.13°, 54.01°, 55.14°, 62.85°, 68.86°, 70.27°, and 75.23° that correspond to the reflections. For Y-doped samples, no additional characteristic peaks other than those of anatase TiO_2 were detected, which may be attributed to the low content and high dispersion of Y species [48]. The broad diffraction peaks indicated that the formed nanoparticles have a very small crystallite size [9, 17, 49–51]. Ahamed et al. reported that the broadening of the reflection peaks to the small grain size of the prepared nanoparticles [52]. Compared with pure (0%) TiO_2, there was a decrease in the intensity of the peaks for the 1% and 5% doped samples. It was reported in the study by Kubiak and Cegłowski that the increase in diffraction peak width as the Y concentration increases indicates that Y ions could be incorporated into the TiO_2 lattice [40]. In a study, Said et al., using XRD patterns of pure and Y/TiO_2 nanoparticles, show that characteristic peaks appear with a wider full width at half maximum (FWHM), and the intensity of the diffraction peaks decreases with increasing Y-doped concentration [53]. Therefore, Y doping (1% and 5%) was observed to effectively restrict crystallite growth (Table 1). The peaks of the powder doped with 10% Y were almost the same as the pure powder and did not show any change. This situation can be attributed to an increase in crystallite growth [54]. A study by Li et al. reported that no diffraction peak shift was observed for Y-modified samples, indicating that Y^{3+} species are located at the crystal boundary or surface of TiO_2, rather than in the internal crystal structure [17].

The crystal size of the Y/TiO_2 powders was determined using the XRD method and the Debye–Scherrer equation (see Equation (1) below) [40, 55].

$$L = \frac{\lambda k}{\beta \cos\theta} \tag{1}$$

In this relation, β is the half-height width of the peak obtained as a result of x-ray diffraction, L is the crystallite size, λ is the wavelength of the applied x-rays, θ is the Bragg angle at which the plane is observed, and K gives a constant value ($K = 0.9$) [56].

The line width was used to estimate the size of the particle by using the Scherrer formula. And, the average crystallite size was estimated using the FWHM of the anatase TiO_2 (101) diffraction peak via Equation (1); instrumental broadening was not corrected, and the reported values are based on a single peak [57].

Using Equation (1), the calculated average crystallite sizes of Y/TiO_2 powders are given in Table 1. The findings demonstrated that the average crystal size for pure (0%), 1%, 5%, and 10% Y/TiO_2 samples was 12.49 nm, 6.28 nm, 5.48 nm, and 11.73 nm, respectively. These results indicate that the crystallite size of pure TiO_2 decreased with Y doping. In particular, the diffraction peaks of the 1% Y/TiO_2 and 5% Y/TiO_2 powders indicate that the formed nanoparticles have very small crystallite sizes. However, although the crystallite size with 10% doping was not as large as with pure TiO_2, its crystallite size increased compared with the 1% and 5% Y-doped samples. Rana et al. have suggested that an increase in crystallite size at higher doping concentrations leads to improved crystallinity, which in turn is reflected in a decrease in microstrain [58]. The addition of 1% and 5% Y^{3+} ions decreases crystallite size due to the formation of OVs, which reduces the lattice parameters and induces strong tensile stress [59, 60]. Also, Y doping prevents the agglomeration between TiO_2 powders and therefore reduces the average crystallite size [61].

The microstrain (ε) [62, 63] value was calculated from Equation (2), and the obtained values are given in Table 1.

$$\varepsilon = \frac{\beta}{4\tan\theta} \tag{2}$$

As a dislocation, the microstrain in the crystal structure affects the material's morphological properties, as well as the formation and size of particles. The dislocation density (δ) was calculated using the Williamson–Smallman relationship [64, 65]. The formula given in Equation (3) was used to calculate the dislocation densities (δ) of the nanoparticles.

$$\delta = \frac{1}{L^2} \tag{3}$$

The average crystallite size, dislocation density, and microstrain of the synthesized TiO_2 powders are summarized in Table 1. It

TABLE 1 | Summary of structural properties of synthesized TiO_2 powders.

Powders	Average crystallite size (nm)	Average microstrain ($\varepsilon \times 10^{-3}$)	Average dislocation density (δ) $\times 10^{-3}$ [lines m^{-2}]
Pure TiO_2	12.49	11.13	12.42
1% Y/TiO_2	6.28	25.04	37.79
5% Y/TiO_2	5.48	27.04	40.12
10%Y/TiO_2	11.73	11.12	12.53

is seen that the dislocation density is inversely proportional to the crystallite size. An average crystallite size (D) was estimated using the Scherrer equation based on the FWHM from the most dominant diffraction peak.

In the study, while a significant decrease in crystal size was observed compared to pure TiO_2 (12.49 nm) with 1% (6.28 nm) and 5% (5.48 nm) doping TiO_2, an increase was observed in average microstrains (pure TiO_2: 11.13, 1% Y/TiO_2: 25.04, and 5% Y/TiO_2: 27.04), and average dislocation densities (pure TiO_2: 12.42 nm, 1% Y/TiO_2: 37.79, and 5% Y/TiO_2: 40.12). This is fully supported by the XRD analysis of the present work [58]. The crystallite size, dislocation density, and microstrain values determined in the study are consistent with those reported in the literature [66–68].

Previous studies reported that it was stated that the strain and dislocation densities increased with increasing doping concentration, and this was attributed to the combination of atoms in the substituted TiO_2 [54]. In another study by Vaddi et al., it was reported that as the Y concentration increased from 0% to 5 mol%, the crystallite size of Y-doped ZnO decreased from 22.9 nm to 19.1 nm, the average crystallite size was smaller for the ZnO: Y_3 nanocatalyst, and the microstrain and dislocation density were greater [65].

3.2 | Morphological Study

3.2.1 | Scanning Electron Microscopy (SEM) Analysis

The morphology of pure and differently doped TiO_2 powders was analyzed. Figure 2a–d shows SEM images of 0%, 1%, 5%, and 10% Y/TiO_2, respectively. It can be seen that the synthesized nanoparticles adhere to each other [69, 70]. While pure TiO_2 exhibited a spherical structure and aggregation, the Y-doped powders showed increased homogeneity and significantly reduced aggregation. This suggests that the Y/TiO_2 powders possess smaller particle sizes compared to pure TiO_2. The SEM analysis revealed that the particles were structurally similar and generally spherical in shape, although perfectly spherical structures were not observed in some regions. This may be attributed to particle agglomeration during the sol–gel synthesis process, which can lead to variations in particle size [71]. It can be said that the concentration, composition of the doped Y ions, or the sol–gel synthesis conditions, are effective in causing agglomeration. As can be seen from the SEM image, the average particle size is consistent with the crystallite size obtained from XRD.

3.2.2 | Energy Dispersive X-ray Spectroscopy (EDS) Analysis

EDS analysis was performed to evaluate the stoichiometry, purity, and incorporation of doped metal ions into the TiO_2 structure following SEM characterization. Measurements were carried out on selected regions of the SEM images, and average elemental compositions were obtained. Figure 3a–d shows the EDS spectra of pure TiO_2 and 1%, 5%, and 10% Y/TiO_2 samples, respectively, along with their corresponding weight and atomic percentages. The results confirm the presence of Y, Ti, and O elements within the samples. After EDS quantification, the measured Y weight percentages for 1%, 5%, and 10% Y/TiO_2 samples were determined as 1.00%, 4.17%, and 3.06%, respectively. The relatively low atomic percentages of Y compared to the nominal doping levels are mainly related to the high atomic mass of yttrium and the semi-quantitative nature of EDS analysis [72]. Nevertheless, both atomic and weight percentage trends are in good agreement with the intended doping levels, indicating successful incorporation of Y into the TiO_2 structure. A gradual increase in Y content was observed up to 5% doping, while a deviation at 10% suggests a limited dopant incorporation, possibly due to the solubility limit of Y in the TiO_2 lattice and local compositional inhomogeneity. No impurity-related signals were detected, confirming the high purity of the synthesized samples. The dominance of Ti and O peaks further supports the formation of the TiO_2 structure. These findings are consistent with XRD results, which confirm that the crystal structure of TiO_2 is preserved after doping, in agreement with previous reports [73].

3.3 | Particle Size Study

Particle size is a crucial factor influencing the performance of nanophotocatalytic materials, as the size and shape of the catalyst affect the surface structure and, consequently, catalytic performance. Figure 4a–d shows the particle size distributions of pure and doped TiO_2 powders measured by DLS. Here, the effect of doping on the average particle size was investigated. The addition of Y led to a decrease in particle size. Accordingly, the smallest particle size was obtained with 5% (50.24 nm) doped Y powder. Although the particle size of the 10% Y-doped sample (215.2 nm) was smaller than that of pure TiO_2 (232.6 nm), it was larger than those of the 1 mol% (192 nm) and 5 mol% (50.24 nm) Y-doped samples. These results are consistent with the SEM and XRD analyses and may be attributed to particle agglomeration at higher doping concentrations [74]. The reduction in nanoparticle size after doping has also been reported in other studies: In their study,

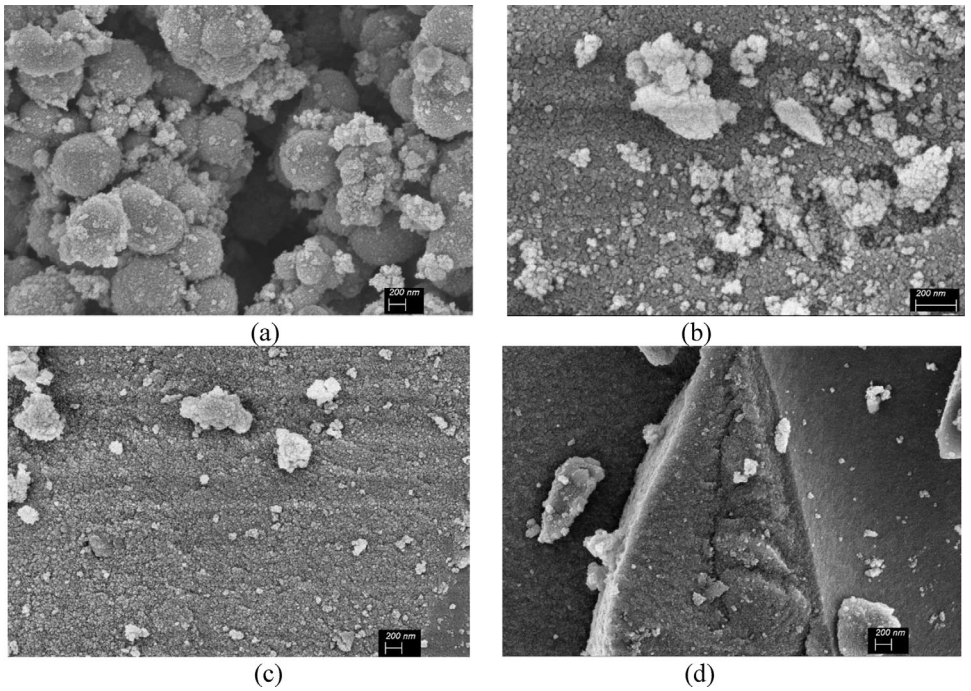

FIGURE 2 | SEM images of TiO_2 powders doped with 0% Y (a), 1% Y (b), 5% Y (c), and 10% Y (d).

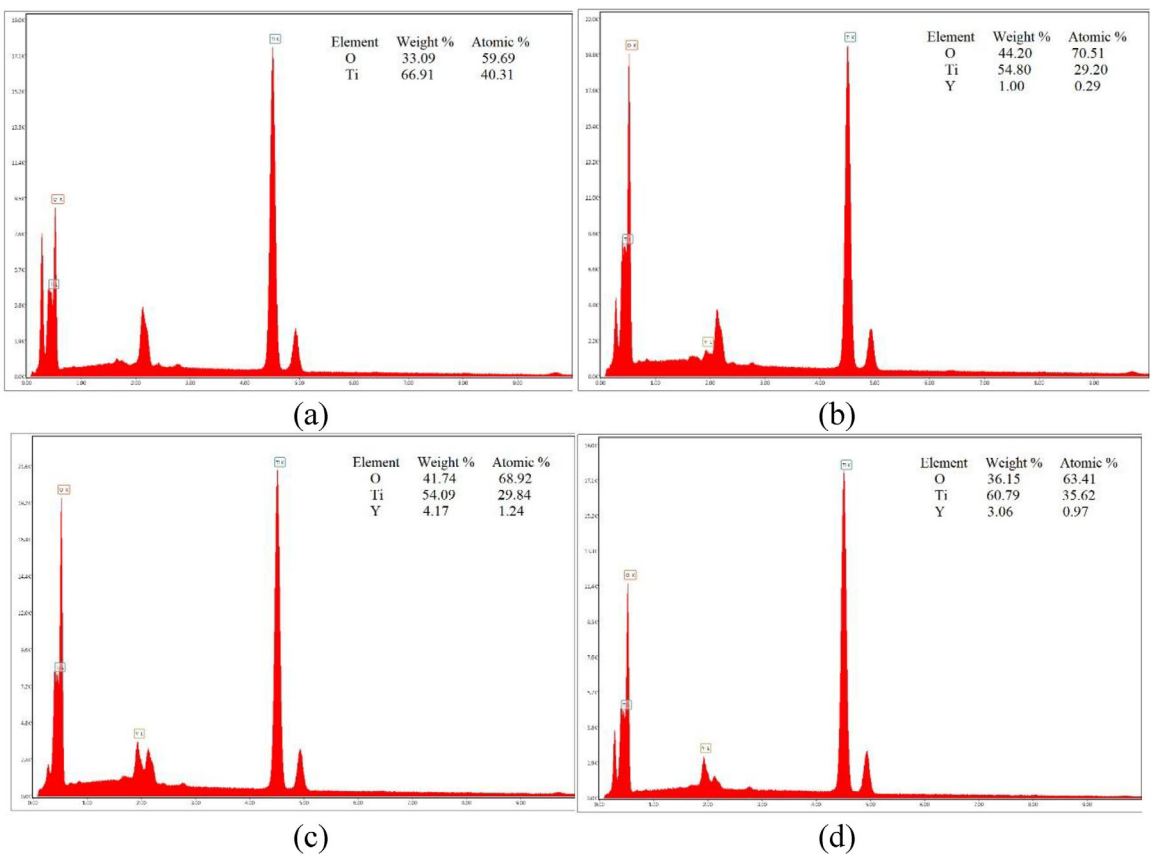

FIGURE 3 | EDS spectra of TiO_2 powders doped with 0% Y (a), 1% Y (b), 5% Y (c), and 10% Y (d).

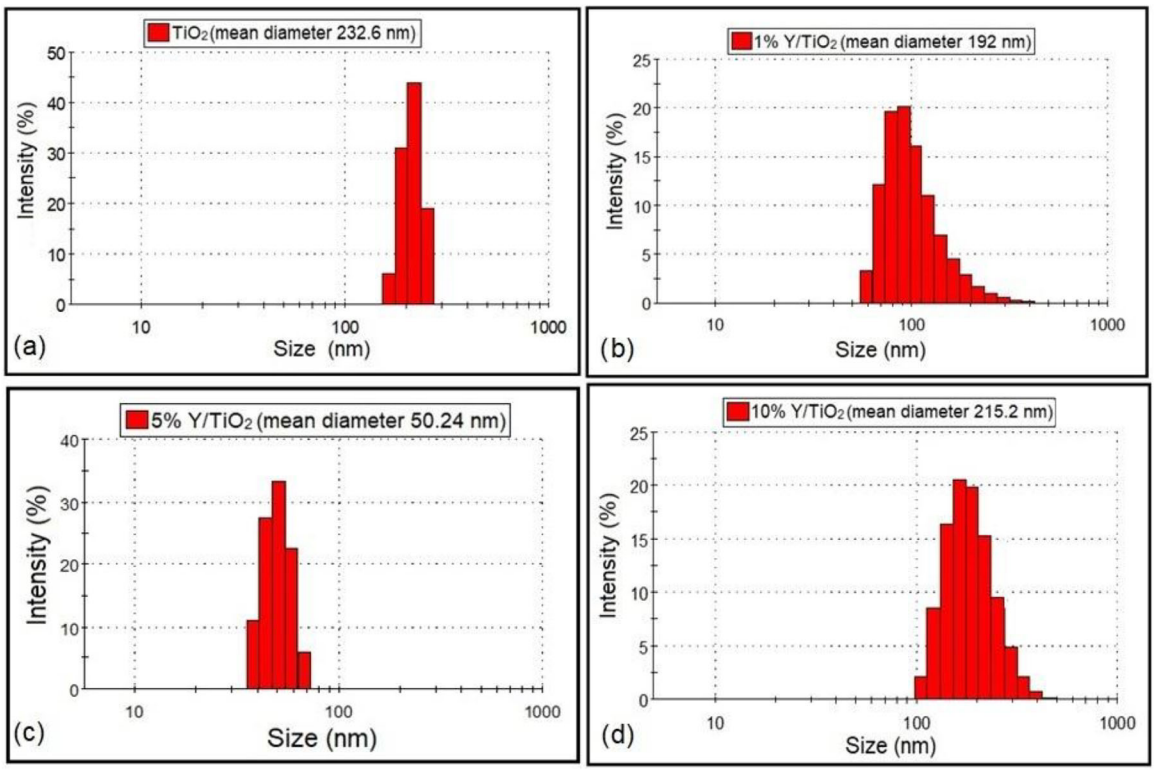

FIGURE 4 | Particle size analyses of TiO_2 nanoparticles doped with 0% Y (a), 1% Y (b), 5% Y (c), and 10% Y (d).

Juárez-Cortazar et al. reported that increasing the amount of dopants in TiO_2 inhibited particle growth; consequently, the pore size distribution became narrower, and the surface area increased [75]. Prabitha et al. discovered that the photocatalytic activity of Y-doped nanoparticles increases as particle size decreases; in their study, they also reported that the increased activity of smaller particles is due to a higher surface area/volume ratio [76]. Kumar et al. showed that the particle sizes decreased from 15.71 nm to 8.8 nm with increasing Y-doping concentration, thus demonstrating that Y-doping reduces nanoparticle size [77].

3.4 | Optic Study

3.4.1 | UV-Visible Analysis

To investigate the optical absorption properties of pure TiO_2 and Y/TiO_2 powders, the UV-vis spectra were recorded in the range 300–800 nm by using a Shimadzu diffuse reflectance UV-vis spectrophotometer. The Kubelka–Munk function was then used to convert these spectra into Tauc Plots, and the following equation was used to get the band gaps.

$$(h\upsilon\alpha)^n = A\left(h\upsilon - E_g\right) \tag{4}$$

Here (Equation (4)), h represents Planck's constant, ν denotes the vibration frequency, α is the absorption coefficient, and E_g refers to the band gap energy. A is a proportionality constant, while n takes the value of 1/2 for an indirectly allowed transition and 2 for a direct allowed transition [8]. The direct and indirect band gap energies of the materials were determined by extending the linear region of the Tauc plots (Figure 5). For TiO_2 powders, the indirect transition model is generally adopted, as it provides a more accurate estimation from the tangent intercept of the $n = 1/2$ plot [8]. No baseline correction was applied before the band gap estimation, and the slight tailing observed near the absorption edge in the UV-Vis spectra of Y/TiO_2 might be attributed to Urbach tail formation caused by dopant-induced localized states, which slightly modifies the optical band gap compared to pure TiO_2 [78–82].

The band gap energies of the doped TiO_2 nanoparticles (E_g) (2.98, 2.86, and 2.9 eV for 1%, 5%, and 10%, respectively) are lower than 3.22 eV for pure TiO_2 (Figure 6). The charge transfer interactions between TiO_2 and yttrium dopant states may be responsible for the observed red shift toward the visible region [73]. Moreover, the variation in band gap with different doping degrees can be attributed to changes in particle size, defect density, and improved structural uniformity at moderate doping concentrations [27].

The 5% Y/TiO_2 sample exhibits the lowest band gap because Y^{3+} provides an optimal effect at this concentration. It promotes better light absorption, increases surface area by reducing particle size and improving morphological uniformity, and introduces beneficial trap states that help reduce electron–hole recombination. However, excessive doping leads to too many defect sites, which act as a recombination center rather than improving charge separation. In addition, dopant agglomeration and possible phase segregation can occur, reducing the effective incorporation of yttrium into the TiO_2 lattice. As a result, the lowest band gap was obtained at the optimal doping concentration of 5% Y/TiO_2.

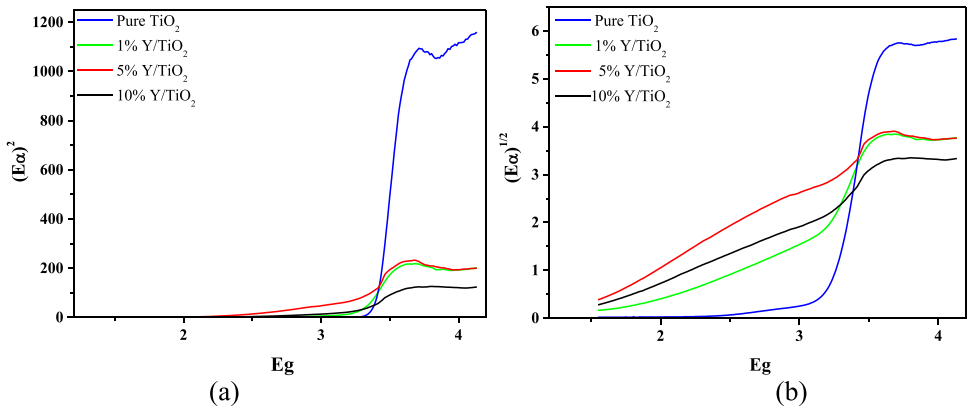

FIGURE 5 | Tauc plots of powders for direct (a) and indirect (b).

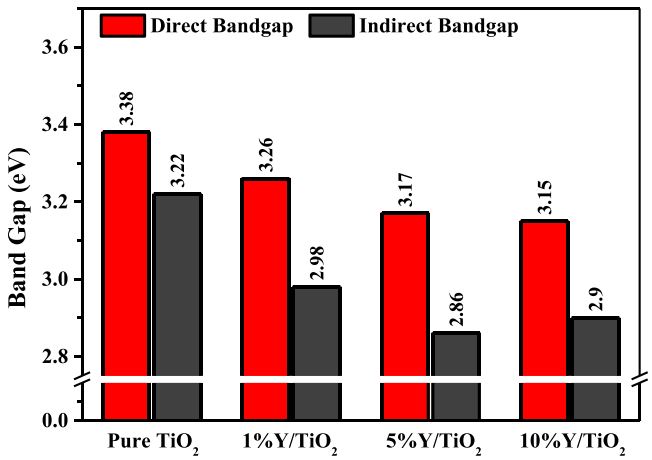

FIGURE 6 | The direct and indirect band gaps of the powders.

3.5 | Photocatalytic Studies

The photocatalytic performance of the TiO_2 powders was evaluated by measuring the rate at which MB, a model organic contaminant, was degraded when the powders were exposed to light. Before illumination, 30 mg of the catalyst powder was dispersed in 30 mL of a 10 mg·L^{-1} MB solution and stirred in the dark at 500 rpm for 30 min to establish adsorption–desorption equilibrium. Following the powders' initial dark UV-Vis spectrum analysis, the UV lamp was turned on, and measurements were made every 30 min until the powders' MB was exhausted (Figure 7). The first measurement in the dark showed that 5% Y/TiO_2 had a higher absorption ability (~40%) than the others. Furthermore, after the photocatalytic measurement, it was observed that the 5% Y/TiO_2 sample performed better when compared to the UV-Vis spectra of all powders. To evaluate the data, the following Equation (5) was used to calculate the MB's degradation ratios [8, 83]:

$$\text{Degradation}\% = [(I_{\text{dark}} - I)/I_{\text{dark}}] \times 100 \quad (5)$$

In this context, I refers to the absorbance intensity recorded at 660 nm at different time intervals during UV illumination, whereas I_{dark} corresponds to the absorbance intensity measured at 660 nm after maintaining the powder in dark conditions for 30 min prior to irradiation. Following 200 min of light illumination, 5% Y/TiO_2 eradicated about 90% of the MB, while the pure TiO_2 degraded about 35% of the MB (Figure 8). A quantitative evaluation of the powders' photocatalytic activity can be achieved by contrasting their apparent reaction rate constants. The Langmuir–Hinshelwood process, a first-order kinetic reaction, is typically followed by photocatalytic degradation and is used to determine the rate constant of each powder (Equation (6)) [8, 84].

$$\ln(C_0/C) = k_a \, .t \quad (6)$$

C_0 represents the initial concentration of MB, while C denotes the MB concentration at various illumination times. These concentrations were determined using a calibration curve constructed from MB solutions of known concentrations prepared from a stock solution of 10 mg. L^{-1}. The calculations were performed according to the Lambert–Beer law ($A = \varepsilon \cdot d \cdot C$), where A is the absorbance, ε is the molar extinction coefficient of the solute at the measurement wavelength, C is the solute concentration, and d is the optical path length [6, 8, 85]. The rate constant is denoted by k, and t denotes time. Among all powders, the 5% Y/TiO_2 catalyst exhibited the highest rate constant (0.01197 min^{-1}), which surpassed those of the other compositions (Figure 9 and Table 2). The photocatalytic efficiency is influenced by factors such as pore size distribution and the energy difference between the valence and conduction bands (band gap). Among the prepared powders, 5% Y/TiO_2 exhibited the smallest band gap and particle size, as confirmed by complementary characterization analyses, including SEM, XRD, and DLS.

The possible improvement in the photocatalytic performance of Y/TiO_2 [27]: (i) it increases UV light absorption and slightly narrows the band gap, which helps reduce electron–hole recombination and improves charge transfer at the surface, (ii) when Y^{3+} replaces Ti^{4+} in the TiO_2 lattice, it suppresses grain growth and increase the surface area that enhance reactivity, (iii) Y^{3+} ions act as electron trap centers inside the TiO_2 structure, slowing down electron–hole recombination (generating more ·OH and $\cdot O_2^-\cdot$ radicals) and thus increasing photocatalytic activity and stability. The optimum doping level was found to be 5% Y/TiO_2, which exhibits the best photocatalytic performance. The concentration of the added metal also plays an important role in photocatalytic activity. It has been suggested that the addition of

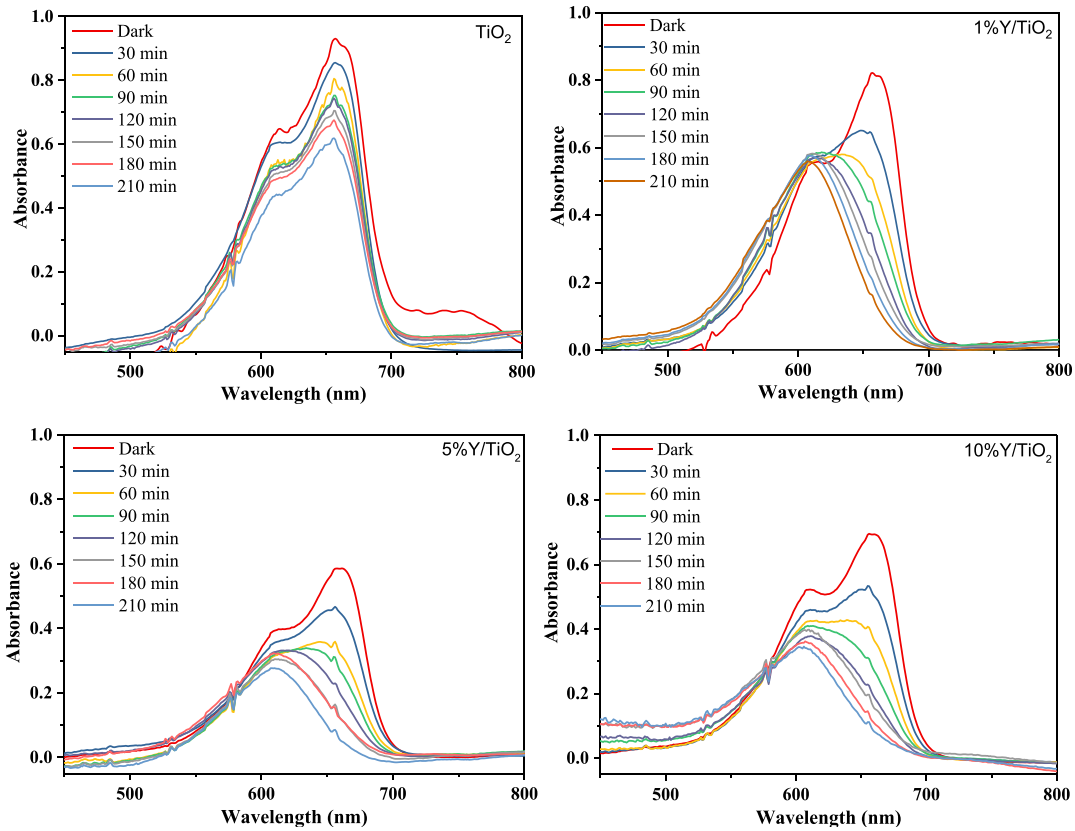

FIGURE 7 | UV-Vis spectra of MB solution at various times, pure TiO_2 (a), 1% Y/TiO_2 (b), 5% Y/TiO_2 (c), and 10% Y/TiO_2 (d).

TABLE 2 | Characteristics of the powders.

Compound	Dark Abs.%	Degradation % of MB at 210 min	E_g (eV) (indirect)	Rate constant (min^{-1})
Pure TiO_2	10.0	35.56	3.22	0.00195
1% Y/TiO_2	19.1	86.42	2.98	0.00943
5% Y/TiO_2	40.9	91.53	2.86	0.01197
10% Y/TiO_2	31.2	87.97	2.90	0.01011

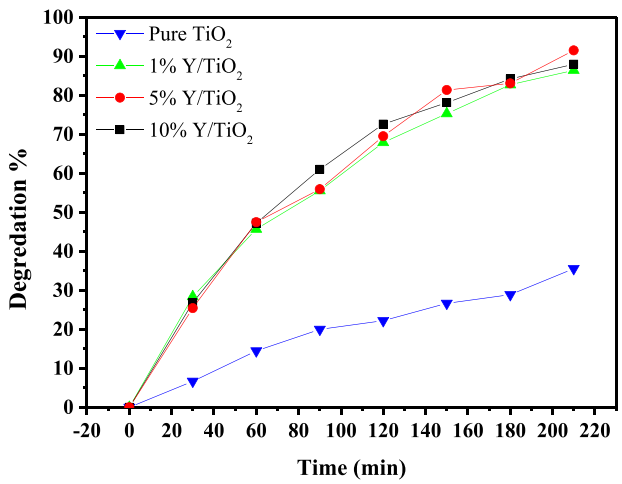

FIGURE 8 | Degradation percentage of MB: This percentage is under light illumination. It shows the percentage for all powders.

some elastic, high-concentration metal ions can cause the decomposition of the transportable active sites in the semiconductor, leading to a decrease in photocatalytic activity [40]. Excessive Y doping can introduce too many defect/trap states in TiO_2 that act as electron-hole recombination centers rather than helping separation, thereby lowering the number of charge carriers available for photocatalytic reactions and reducing activity [27, 30, 73]. Moreover, the agglomerated particles observed in the SEM images may have reduced the photocatalytic performance of the 10% doped powders through light quenching.

Some studies have reported on the photocatalytic activity of Y/TiO_2; however, many of these systems also include additional modifiers such as carbon, Au, and GO (graphene oxide) [73, 86]. While enhanced photocatalytic performance is often observed, these additives already contribute significantly to photoactivity, and the incorporation of Y further improves the overall performance (increasing degradation from 65.21% for pure TiO_2 to 89.95% for TiO_2:GO, and further to 91.45% for TiO_2:GO:0.3Y)

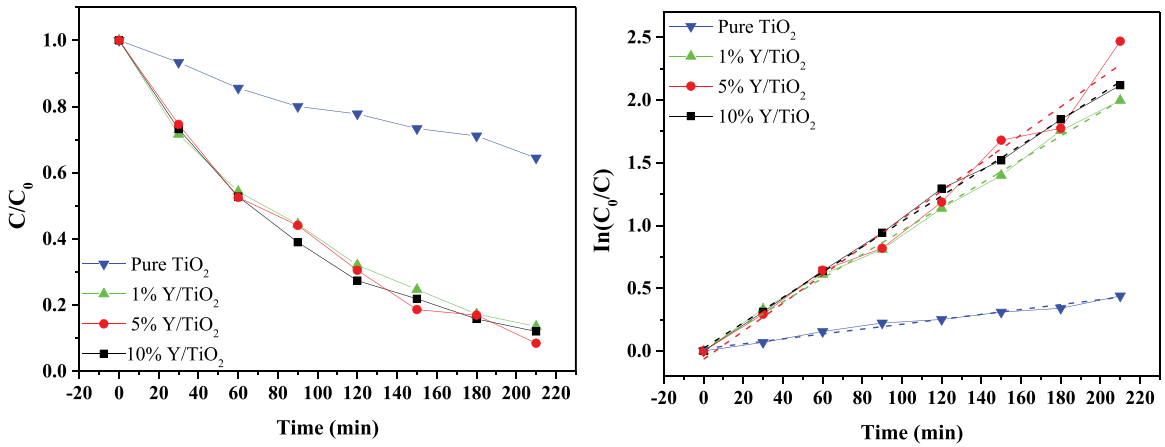

FIGURE 9 | (a) Degradation curve of MB under the light illumination for all powders. (b) Degradation curve of MB under the light illumination for synthesized TiO_2 powders.

[73]. To the best of our knowledge, achieving 91.53% degradation with 5% Y/TiO_2 without additional modifiers (compared to the 35% degradation observed in the pure TiO_2) represents a highly competitive result when both low doping concentration and high degradation efficiency are considered [27].

4 | Conclusions

Pure TiO_2 (0%), 1% Y/TiO_2, 5% Y/TiO_2, and 10% Y/TiO_2 powders were successfully synthesized via the sol-gel method. The effects of Y doping on the structural, morphological, chemical, and photocatalytic properties of TiO_2 powders were investigated using XRD, SEM/EDS, particle size analysis, and UV-Vis spectroscopy. In the XRD patterns, all samples exhibited the anatase TiO_2 (101) peak at $2\theta \approx 25.3°$, and no additional Y-related phases were detected, indicating that Y^{3+} ions were highly dispersed or present in low concentrations. While 1% and 5% Y doping reduced peak intensity and crystallite size due to lattice distortion, this effect was less pronounced at the10% Y doping level, suggesting limited incorporation of Y into the TiO_2 lattice and possible segregation at the surface or grain boundaries. The average crystallite sizes of all powders were determined using Scherrer's equation. SEM images revealed that the synthesized powders possessed a spherical morphology with a homogeneous particle distribution. EDS analyses showed high-intensity Ti, O, and Y peaks, and no impurity phases were detected. The properties of the synthesized powders were found to be in good agreement with the literature. It was suggested that the 10% Y-doped sample contained a lower effective incorporation of Y in the TiO_2 lattice, which could reduce the number of active sites on the semiconductor surface and consequently lead to decreased photocatalytic activity. Particle size analysis confirmed that Y doping reduced the particle size of TiO_2. UV-Vis results showed that the band gap decreased from 3.22 eV (pure TiO_2) to a minimum of 2.86 eV at 5% Y doping, followed by a slight increase at higher doping levels, indicating an optimal Y concentration for band gap narrowing. These findings, which align well with the literature, are supported by SEM, XRD, and DLS results, which also confirm that 5% Y/TiO_2 exhibits the smallest particle size and most favorable structural properties. Photocatalytic activity studies demonstrated that the addition of Y dopant to titanium dioxide led to a significant improvement in its photocatalytic performance. The highest degradation efficiency was observed for 5% Y/TiO_2, which degraded approximately 91% of MB, while pure TiO_2 degraded about 35% of MB. The increased photoactivity of 5% Y/TiO_2 is attributed to a reduced band gap, increased visible light absorption, and improved separation of electron–hole pairs.

In conclusion, different Y doping concentrations significantly affected particle size, band gap, and photocatalytic activity. Optical studies showed a substantial narrowing of the band gap and the emergence of new energy states within the TiO_2 matrix at a 5% Y doping ratio. These results suggest that the synthesized doped TiO_2 materials hold significant promise for solar cell applications, offering valuable insights for future research in this field.

Funding

The authors have nothing to report.

Data Availability Statement

The data that support the findings of this study are available from the corresponding author upon reasonable request.

References

1. H. A. Hasan, N. A. Jabir, H. A. Hussin, et al., "Enhanced Efficiency of Undoped and Ag-Doped ZnO Nanostructure for Sustainable Dye-Sensitized Solar Cells," *Journal of Electronic Materials* 55 (2026): 2791–2802, https://doi.org/10.1007/s11664-026-12675-7.

2. S. M. Mirkazemi and A. M. AArabi, "Synergistic Effect of $CoFe_2O_4$ and Ag Nanoparticles on TiO_2 Photoanodes for High-Efficiency Dye-Sensitized Solar Cells With and Without External Magnetic Field," *Materials Science and Engineering: B* 327 (2026): 119264, https://doi.org/10.1016/j.mseb.2026.119264.

3. X. Li, S. Li, C. Dai, C. Lan, and M. Guli, "Advances in Organic Acid Compounds Modification of SnO_2 Electron Transport Layer for Perovskite Solar Cells," *Journal of Power Sources* 672 (2026): 239639, https://doi.org/10.1016/j.jpowsour.2026.239639.

4. Y. R. Ho, C. N. Chen, J. Z. Chen, and J. J. Huang, "Electrochemically Deposited SnO_2–TiO_2 Compact Layers for Enhanced Carrier Transport and Defect Passivation in Dye-Sensitized Solar Cells," *Materials Science*

and Engineering: B 328 (2026): 119357, https://doi.org/10.1016/j.mseb.2026.119357.

5. M. Sangari, "Photocatalytic Activity of Cu Doped TiO_2 Synthesized by Sonochemical Method", *International Journal of Engineering Science Invention* ISSN (Online): 2319 –6734, ISSN (Print): 2319 –6726 (2017): 66–69, Access date: March 31, 2026. https://www.ijesi.org/papers/ICAFM-2017/Volume-1/10.%2064-66.pdf.

6. D. V. Aware and S. S. Jadhav, "Synthesis, Characterization and Photocatalytic Applications of Zn-doped TiO_2 Nanoparticles by Sol–Gel Method," *Applied Nanoscience* 6, no. 7 (2016): 965–972, https://doi.org/10.1007/s13204-015-0513-8.

7. M. Nisar, N. Khan, M. L. Qadir, and Z. Shah, "Recent Advances in TiO_2-based Photocatalysts for Efficient Water Splitting to Hydrogen," *Nanomaterials* 15, no. 13 (2025): 984, https://doi.org/10.3390/nano15130984.

8. F. A. Unal, S. Ok, M. Unal, S. Topal, K. Cellat, and F. Şen, "Synthesis, Characterization, and Application of Transition Metals (Ni, Zr, and Fe) Doped TiO_2 Photoelectrodes for Dye-Sensitized Solar Cells," *Journal of Molecular Liquids* 299 (2020): 112177, https://doi.org/10.1016/j.molliq.2019.112177.

9. A. Mikolajczyk, E. Wyrzykowska, P. Mazierski, et al., "Visible-light Photocatalytic Activity of Rare-Earth-Metal-Doped TiO_2: Experimental Analysis and Machine Learning for Virtual Design," *Applied Catalysis B: Environment and Energy* 346 (2024): 123744, https://doi.org/10.1016/j.apcatb.2024.123744.

10. Y. Sheng, L. Liang, Y. Xu, D. Wu, and Y. Sun, "Low-Temperature Deposition of the High-Performance Anatase-Titania Optical Films via a Modified Sol–Gel Route," *Optical Materials* 30, no. 8 (2008): 1310–1315, https://doi.org/10.1016/j.optmat.2007.06.010.

11. D. R. Eddy, M. D. Permana, L. K. Sakti, et al., "Heterophase Polymorph of TiO_2 (Anatase, Rutile, Brookite, TiO_2 (B)) for Efficient Photocatalyst: Fabrication and Activity," *Nanomaterials* 13, no. 4 (2023): 704, https://doi.org/10.3390/nano13040704.

12. W. Nachit, H. Ait Ahsaine, Z. Ramzi, S. Touhtouh, I. Goncharova, and K. Benkhouja, "Photocatalytic Activity of Anatase-Brookite TiO_2 Nanoparticles Synthesized by Sol Gel Method at Low Temperature," *Optical Materials* 129 (2022): 112256, https://doi.org/10.1016/j.optmat.2022.112256.

13. K. Nagaraj, S. Radha, C. G. Deepa, et al., "Photocatalytic Advancements and Applications of Titanium Dioxide (TiO_2): Progress in Biomedical, Environmental, and Energy Sustainability," *Next Research* 2, no. 1 (2025): 100180, https://doi.org/10.1016/j.nexres.2025.100180.

14. X. Zhang and Y. Ma, "Towards High-Efficiency Photocatalytic TiO_2 Nanosheets: Mechanisms, Modifications, and Breakthroughs," *Physical Chemistry Chemical Physics* 27, no. 34 (2025): 17630–17651, Y., https://doi.org/10.1039/D5CP00939A.

15. B. Caliskan, E. Sayan, and E. Igman, "Exploring the Role of Rare Earth Elements Doped TiO_2 Based Photoanodes on the Performance of Dye-sensitized Solar Cells," *Journal of Sol-Gel Science and Technology* 118, no. 1 (2026): 6, https://doi.org/10.1007/s10971-026-07134-y.

16. Y. Wang, Y. Zhu, and Y. Xia, "Metal–Organic Frameworks Derived $Cu_xO/TiO_2/C$ Nanocomposites With Enhanced Photocatalytic Performance," *Advanced Energy and Sustainability Research* 7, no. 1 (2026): e202500411, https://doi.org/10.1002/aesr.202500411.

17. X. Li, H. Zheng, Y. Wang, et al., "Synergistic Effect of Y Doping and Reduction of TiO_2 on the Improvement of Photocatalytic Performance," *Nanomaterials* 13, no. 15 (2023): 2266, https://doi.org/10.3390/nano13152266.

18. P. K. Sanoop, S. Anas, S. Ananthakumar, V. Gunasekar, R. Saravanan, and V. Ponnusami, "Synthesis of Yttrium Doped Nanocrystalline ZnO and Its Photocatalytic Activity in Methylene Blue Degradation," *Arabian Journal of Chemistry* 9 (2016): S1618–S1626, https://doi.org/10.1016/j.arabjc.2012.04.023.

19. L. Yu, Y. Duan, D. Wang, Z. Liang, C. Liang, and Y. Wang, "Recent Advances in TiO_2 Modification for Improvement in Photocatalytic Purification of Indoor VOCs," *RSC Advances* 15, no. 34 (2025): 28204–28230, https://doi.org/10.1039/D5RA02935J.

20. S. M. Mustafa, "Green Solvent-Based Synthesis of Sm^{3+}-Doped TiO_2 Nanostructures for Solar Energy Conversion," *Journal of Molecular Structure* 1345 (2025): 143137, https://doi.org/10.1016/j.molstruc.2025.143137.

21. V. Verma and S. V. Singh, "La-Doped TiO_2 Nanoparticles for Photocatalysis: Synthesis, Activity in Terms of Degradation of Methylene Blue Dye and Regeneration of Used Nanoparticles," *Arabian Journal for Science and Engineering* 48, no. 12 (2023): 16431–16443, https://doi.org/10.1007/s13369-023-08325-3.

22. P. Lian, A. Qin, Z. Liu, et al., "One-Step Synthesis of Nitrogen-Doped TiO_2 Heterojunctions and Their Visible Light Catalytic Applications," *Materials* 18, no. 10 (2025): 2400, https://doi.org/10.3390/ma18102400.

23. K. Greeshma, A. K. Adiyodi, S. S. Ancy, S. P. Dhale, N. S. Ugemuge, and K. M. Nissamudeen, "Synthesis and Spectroscopic Analysis of TiO_2: Dy^{3+} Phosphor for Optical and Pharmaceutical Applications," *Spectrochimica Acta Part A: Molecular and Biomolecular Spectroscopy* 337 (2025): 126086, https://doi.org/10.1016/j.saa.2025.126086.

24. E. Aghababaei, M. Alizadeh, and A. Bahrami, "Synthesis and Characterization of Ce-Doped TiO_2/Cu-Doped Fe_3O_4 Heterogeneous Photocatalyst for Antibacterial Applications and Visible-Light Photocatalytic Degradation of Methylene Blue," *Ceramics International* 51, no. 21 (2025): 33740–33758, https://doi.org/10.1016/j.ceramint.2025.05.109.

25. S. N. Awandkar, Y. S. Patil, S. A. Deshmukh, J. H. Kim, and G. L. Agawane, "Rare Earth-Doped TiO 2 for Enhanced Photocatalytic Performance," *ChemNanoMat* 12, no. 1 (2026): e202500467, https://doi.org/10.1002/cnma.202500467.

26. Z. Guan and P. Zhou, "Research and Analysis of the Photocatalytic Performance of Rare Earth Element-Doped TiO_2," in *Fourth International Conference on Advanced Materials and Equipment Manufacturing* 14144 (2026), 361–366, https://doi.org/10.1117/12.3107093.

27. P. Rajput, M. P. Deshpande, H. R. Bhoi, et al., "Photocatalytic and Antibacterial Activity of Yttrium Doped TiO_2 Nanostructure," *Chemical Physics Impact* 5 (2022): 100101, https://doi.org/10.1016/j.chphi.2022.100101.

28. L. Hou, L. Xia, R. Zhou, et al., "Effect of Yttrium on Catalytic Performance of Y-doped TiO_2 Catalysts for Propane Dehydrogenation," *Journal of Rare Earths* 42, no. 5 (2024): 962–971, https://doi.org/10.1016/j.jre.2023.03.007.

29. Y. Li, Z. Fang, L. Feng, et al., "Study of Mesoporous Zr-TiO_2 Catalyst With Rich Oxygen Vacancies for N-Methylmorpholine Oxidation to N-Methylmorpholine-N-Oxide," *Molecules* 29, no. 16 (2024): 3812, https://doi.org/10.3390/molecules29163812.

30. J. Rao, H. Xue, W. Zhang, X. Li, X. You, and Z. Xing, "Synthesis of Yttrium Doped TiO_2 Nanotubes by a Microwave Refluxing Method and Their Photoluminescence Properties and Photocatalytic Properties," *International Journal of Electrochemical Science* 11, no. 3 (2016): 2408–2418, https://doi.org/10.1016/S1452-3981(23)16113-X.

31. A. Namoune, D. Djouadi, T. Touam, K. Ikkour, and A. Chelouche, "Effect of Yttrium Co-Doping on the Microstructure, Optical Properties, and Photocatalytic Activity of Al-Doped TiO_2 Nanostructures," *Russian Journal of Physical Chemistry B* 20 (2026): 326–337, https://doi.org/10.1134/S1990793125701696.

32. Z. Wang, B. Wang, L. Zhang, and J. Li, "Study on the Synthesis of Multi-Walled Carbon Nanotube-Supported La-N Co-Doped TiO_2 and Its Coupled Photocatalytic Degradation of Rhodamine B (RhB)," *Journal of Sol-Gel Science and Technology* 117, no. 1 (2026): 5, https://doi.org/10.1007/s10971-025-07020-z.

33. T. Zhang, G. Sa, and A. Xu, "Photocatalytic Degradation of Phenol With One-Step Hydrothermal Synthesized Bi-TiO_2," *Vacuum* 233 (2025): 113982, https://doi.org/10.1016/j.vacuum.2024.113982.

34. M. T. Abdu, "Harnessing Mesoporosity and Nitrogen Doping to Engineer a Superior Carbon-TiO_2 Photocatalyst for Methylene Blue Degradation," *RSC Advances* 16, no. 4 (2026): 3712–3719, https://doi.org/10.1002/cnma.202500467.

35. R. Ueda, T. Sudare, R. Shimizu, et al., "Anatase TiO_2 (112) Epitaxial Thin Films Grown by Mist Chemical Vapor Deposition," *Crystal Growth & Design* 25, no. 21 (2025): 9086–9091, https://pubs.acs.org/doi/10.1021/acs.cgd.5c00986.

36. S. U. Hiwale, K. M. Chavan, V. A. Mane, et al., "Enhanced Visible-Light Photocatalysis via TiO_2-Based Ni-Doped ZnO Nanocomposites for Sustainable Dye Degradation," *Physica Status Solidi A: Applications and Materials Science* 223 (2026): e202500742, https://doi.org/10.1002/pssa.202500742op.

37. B. A. Abbas, N. J. Ridha, K. J. Tahir, and M. H. Jumali, "Influence of Ag and Au Doping Ratio on TiO₂ Nanostructures Synthesized by the Solvothermal Method," *Journal of Nano Research* 92 (2026): 57–74, https://doi.org/10.4028/p-i9bhCw.

38. S. Baïlo Diallo, N. Khlifi, M. Fall, and H. Guermazi, "Tunable Structure–Property Engineering and Visible-Light Photocatalytic Performance of ZnO: TiO_2 Nanocomposites Synthesized via a Solid-State Route," *RSC Advances* 16, no. 5 (2026): 4090–4106, https://doi.org/10.1039/D5RA08953K.

39. Frendi Maulana and Yohanes Engge, "Study of Photocatalytic Hydrogen Production Over Ni-Doped ZnO and TiO_2 Photocatalysts via Chemical Stabilization," *Multidisciplinary Indonesian Center Journal (MICJO)* 3, no. 1 (2026): 2329–2341, https://doi.org/10.62567/micjo.v3i1.2314.

40. A. Kubiak and M. Cegłowski, "Unraveling the Impact of Microwave-Assisted Techniques in the Fabrication of Yttrium-Doped TiO_2 Photocatalyst," *Scientific Reports* 14, no. 1 (2024): 262, https://doi.org/10.1038/s41598-023-51078-0.

41. G. B. Stelzer, I. C. Prescilio, L. G. Vasconcelos, A. F. Bakuzis, and M. J. Jacinto, "A Green Sol–Gel Route to Fe_3O_4@ TiO_2–CuO Photocatalysts With Structural Stability, Visible–Light Activity, and Magnetic Recoverability," *ACS Omega* (2026): 15942–15955, https://pubs.acs.org/doi/10.1021/acsomega.5c09939.

42. C. Subhayu, "A Review of the Sol-Gel Process and Its Application," *International Education and Research Journal (IERJ)* 10, no. 7 (2024): 454–9916, https://doi.org/10.21276/IERJ24449856325648.

43. M. Murthi and J. F. Destino, "Sol-Gel Technologies for Additive Manufacturing Glass Materials," *Journal of Sol-Gel Science and Technology* 116, no. 3 (2025): 2257–2271, https://doi.org/10.1007/s10971-025-06743-3.

44. P. Yapa and I. Munaweera, "Functionalized Nanoporous Architectures Derived From Sol–Gel Processes for Advanced Biomedical Applications," *Journal of Materials Chemistry B* 13, no. 35 (2025): 10715–10742, https://doi.org/10.1039/D5TB00958H.

45. A. N. Tuama, L. H. Alzubaidi, M. H. Jameel, K. H. Abass, M. Z. H. bin Mayzan, and Z. N. Salman, "Impact of Electron–Hole Recombination Mechanism on the Photocatalytic Performance of ZnO in Water Treatment: A Review," *Journal of Sol-Gel Science and Technology* 110, no. 3 (2024): 792–806, https://doi.org/10.1007/s10971-024-06385-x.

46. S. K. Sivan, S. S. Shankar, S. N, et al., "Fabrication of a Greener TiO_2@ Gum Arabic-Carbon Paste Electrode for the Electrochemical Detection of Pb^{2+} Ions in Plastic Toys," *ACS Omega* 5, no. 39 (2020): 25390–25399, https://dx.doi.org/10.1021/acsomega.0c03781.

47. S. Haque, M. M. Khan, M. S. Jahan, et al., "Rare Earth Doped TiO_2 Thin Film: A Review on Structural, Optical, Photocatalytic, Magnetic, and Electrical Properties," *Next Materials* 11 (2026): 101661, https://doi.org/10.1016/j.nxmate.2026.101661.

48. X. Qu, Y. Hou, M. Liu, et al., "Yttrium Doped TiO_2 Porous Film Photoanode for Dye-Sensitized Solar Cells With Enhanced Photovoltaic Performance," *Results in Physics* 6 (2016): 1051–1058, https://doi.org/10.1016/j.rinp.2016.11.021.

49. Z. Hamden, D. Conceição, S. Boufi, L. F. Vieira Ferreira, and S. Bouattour, "Structural, Morphological, Optical and Photocatalytic Properties of Y, N-Doped and Codoped TiO_2 Thin Films," *Materials* 10, no. 6 (2017): 600, https://doi.org/10.3390/ma10060600.

50. K. M. Elattar, N. M. Askar, N. H. Elhusseini, et al., "Green Synthesis of Ag/TiO_2 and Ag/Co/TiO_2 Nanocomposites From Ceratonia Siliqua Extract for Antioxidant and Antibacterial Applications," *ChemistrySelect* 10, no. 38 (2025): e03394, https://doi.org/10.1002/slct.202503394.

51. O. Ouerghi, M. H. Geesi, E. O. H. Riadi, E. O. Ibnouf, and A. Kaiba, "Phytosynthesis of Anatase TiO_2 Nanostructures Using Grapefruit Extract for Antimicrobial and Catalytic Applications," *Journal of Sol-Gel Science and Technology* 108, no. 2 (2023): 538–547, https://doi.org/10.1007/s10971-023-06215-6.

52. M. Ahamed, M. M. Khan, M. J. Akhtar, H. A. Alhadlaq, and A. Alshamsan, "Ag-Doping Regulates the Cytotoxicity of TiO_2 Nanoparticles via Oxidative Stress in Human Cancer Cells," *Scientific Reports* 7, no. 1 (2017): 17662, https://doi.org/10.1038/s41598-017-17559-9.

53. K. E. Lakshmiprabha, T. F. Gladson, V. Chithambaram, S. Yogeeswaran, M. T. Alotaibi, and S. S. J. Dhas, "Tailoring Yttrium-Doped TiO_2 Using Natural Dye From Flowers of Pomegranate in the Fabrication of a Dye-Sensitized Solar Cell: An Investigation," *Optical and Quantum Electronics* 57, no. 9 (2025): 493, https://doi.org/10.1007/s11082-025-08417-4.

54. N. D. Mohd Said, M. Z. Sahdan, N. Nayan, et al., "Difference in Structural and Chemical Properties of Sol–Gel Spin Coated Al Doped TiO_2, Y Doped TiO_2 and Gd Doped TiO_2 Based on Trivalent Dopants," *RSC advances* 8, no. 52 (2018): 29686–29697, https://doi.org/10.1039/C8RA03950J.

55. O. Zuas, F. A. Dzakirah, and T. Sudiro, "Harnessing Sterculia Foetida Seed Coat for Silver Nanoparticles Biofabrication: Characterization and a Rapid, Highly Efficient Catalyst for Methylene Blue Degradation," *Biointerface Research in Applied Chemistr* 15, no. 3 (2025): 38, https://doi.org/10.33263/BRIAC153.038.

56. A. A. Dakhel and M. El-Hilo, "Ferromagnetic Nanocrystalline Gd-Doped ZnO Powder Synthesized by Coprecipitation," *Journal of Applied Physics* 107 (2010): 123905, https://doi.org/10.1063/1.3448026.

57. A. El Mragui, Y. Logvina, L. Pinto da Silva, O. Zegaoui, and J. CG Esteves da Silva, "Synthesis of Fe- and Co-Doped TiO_2 With Improved Photocatalytic Activity Under Visible Irradiation Toward Carbamazepine Degradation," *Materials (Basel)* 12, no. 23 (2019): 3874, 24, https://doi.org/10.3390/ma12233874.

58. P. Rana, M. E. Islam, S. Tabassum, and A. B. M. Ismail, "Nickel Doping Induced Morphological and Structural Transformation of Electrochemically Deposited ZnO Nanostructures via Ethylene Glycol Based Electrolyte," *Scientific Reports* 15, no. 1 (2025): 34012, https://doi.org/10.1038/s41598-025-13516-z.

59. N. Aggarwal, K. Kaur, A. Vasishth, and N. K. Verma, "Structural, Optical, and Magnetic Properties of Gadolinium-Doped ZnO Nanoparticles," *Journal of Materials Science: Materials in Electronics* 27 (2016): 13006–13011, https://doi.org/10.1007/s10854-016-5440-2.

60. S. Agarwal, L. K. Jangir, K. S. Rathore, M. Kumar, and K. Awasthi, "Morphology-Dependent Structural and Optical Properties of ZnO Nanostructures," *Applied Physics A* 125 (2019): 1–7, https://doi.org/10.1007/s00339-019-2852-x.

61. X. Yao, W. Dai, Q. Wang, and J. Wang, "Influence of Y Doping on High Temperature Oxidation Resistance of Titanium Diboride Coatings," *Journal of Materials Research and Technology* 37 (2025): 5003–5016, https://doi.org/10.1016/j.jmrt.2025.07.148.

62. A. T. Salih, A. A. Najim, M. A. Muhi, and K. R. Gbashi, "Single-Material Multilayer ZnS as Anti-Reflective Coating for Solar Cell Applications," *Optics Communications* 388 (2017): 84–89, https://doi.org/10.1016/j.optcom.2016.12.035.

63. M. Dongol, A. El-Denglawey, M. S. Abd El Sadek, and I. S. Yahia, "Thermal Annealing Effect on the Structural and the Optical Properties of Nano CdTe Films," *Optik* 126 (2015): 1352–1357, https://doi.org/10.1016/j.ijleo.2015.04.048.

64. N. Kati and B. Ayten, "Investigation of Structural and Optical Properties of Boron-Doped ZnO Nanomaterials Synthesized by Hydrothermal Method," *Journal of the Indian Chemical Society* 102, no. 6 (2025): 101706, https://doi.org/10.1016/j.jics.2025.101706.

65. D. R. Vaddi, K. Vinukonda, R. K. Patnala, et al., "Effect of Yttrium Doping on the Crystal Structure, Optical, and Photocatalytic Properties of Hydrothermally Synthesized ZnO Nanorods," *Materials Science and Engineering: B* 296 (2023): 116664, https://doi.org/10.1016/j.mseb.2023.116664.

66. C. A. Prabhu, D. Silambarasan, R. Sarika, and V. Selvam, "Synthesis and Characterization of TiO_2," *Materials Today: Proceedings* 64 (2022): 1793–1797, https://doi.org/10.1016/j.matpr.2022.06.074.

67. K. Ullah, S. A. Khan, A. Zaman, et al., "Impact of Cobalt Doping on the Structural, Optical, and Dielectric Properties of $MgAl_2O_4$ Spinel Material," *ACS Omega* 8, no. 33 (2023): 29959–29965, https://doi.org/10.1021/acsomega.3c00541.

68. K. Igenepo John, A. Abdul Adenle, A. Timothy Adeleye, I. Pearl Onyia, C. Amune-Matthews, and M. O. Omorogie, "Unravelling the Effect of Crystal Dislocation Density and Microstrain of Titanium Dioxide Nanoparticles on Tetracycline Removal Performance," *Chemical Physics Letters* 776 (2021): 138725, https://doi.org/10.1016/j.cplett.2021.138725.

69. A. M. Sharif, M. Ashrafuzzaman, A. Kalam, et al., "Green Synthesis of Pristine and Ag-Doped TiO_2 and Investigation of Their Performance as Photoanodes in Dye-Sensitized Solar Cells," *Materials* 16, no. 17 (2023): 5731, https://doi.org/10.3390/ma16175731.

70. M. Al-Zu'bi, L. Anguilano, and M. Fan, "Effect of Incorporating Carbon-and Silicon-Based Nanomaterials on the Physico-Chemical Properties of a Structural Epoxy Adhesive," *Polymer Testing* 128 (2023): 108221, https://doi.org/10.1016/j.polymertesting.2023.108221.

71. J. C. Yu, Yu, Ho, Jiang, and Zhang, "Effects of F—Doping on the Photocatalytic Activity and Microstructures of Nanocrystalline TiO 2 Powders," *Chemistry of Materials* 14, no. 9 (2002): 3808–3816, https://doi.org/10.1002/chin.200247012.

72. A. R. Goldstein, D. E. Newbury, and P. Echlin, *A Beginner's Guide to Scanning Electron Microscopy* (Springer Science & Business Media, 2017).

73. N. Y. Devi, K. Janarthana Karthikeyan, F. Oleyan Al-Otibi, et al., "Effect of Yttrium Doping on Enhancing the Photocatalytic Performance of TiO_2/GO Nanocomposite," *Optical Materials* 155 (2024): 115791, https://doi.org/10.1016/j.optmat.2024.115791.

74. N. M. Al-Hada, R. M. Kasmani, H. Kasim, et al., "The Effect of Precursor Concentration on the Particle Size, Crystal Size, and Optical Energy Gap of $Ce_xSn_{1-x}O_2$ Nanofabrication," *Nanomaterials* 11, no. 8 (2021): 2143, https://doi.org/10.3390/ma15092996.

75. D. E. Juárez-Cortazar, J. G. Torres-Torres, A. Hernandez-Ramirez, et al., "Doping of TiO_2 Using Metal Waste (Door Key) to Improve Its Photocatalytic Efficiency in the Mineralization of an Emerging Contaminant in an Aqueous Environment," *Water* 14, no. 9 (2022): 1389, https://doi.org/10.3390/w14091389.

76. V. G. Prabitha, J. Sahadevan, M. Madhavan, et al., "Effect of Yttrium Doping on Antibacterial and Antioxidant Property of $LaTiO_3$," *Discover Nano* 18, no. 1 (2023): 155, https://doi.org/10.1186/s11671-023-03942-1.

77. K. S. Kumar, C. G. Song, G. M. Bak, G. Heo, M. J. Seong, and J. W. Yoon, "Phase Control of Yttrium (Y)-Doped TiO_2 Nanofibers and Intensive Visible Photoluminescence," *Journal of Alloys and Compounds* 617 (2014): 683–687, https://doi.org/10.1016/j.jallcom.2014.08.067.

78. B. Choudhury and A. Choudhury, "Oxygen Defect Dependent Variation of Band Gap, Urbach Energy and Luminescence Property of Anatase, Anatase–rutile Mixed Phase and of Rutile Phases of TiO2 Nanoparticles," *Physica E: Low-Dimensional Systems and Nanostructures* 56 (2014): 364–371, https://doi.org/10.1016/j.physe.2013.10.014.

79. I. Y. Bouderbala, A. Guessoum, S. Rabhi, O. Bouhlassa, and I. E. Bouras, "Optical Band-Diagram, Urbach Energy Tails Associated With Photoluminescence Emission in Defected ZnO Thin Films Deposited by Sol–Gel Process Dip-Coating: Effect of Precursor Concentration," *Applied Physics A* 130, no. 3 (2024): 205, https://doi.org/10.1007/s00339-024-07366-1.

80. A. V. Subashiev, O. Semyonov, Z. Chen, and S. Luryi, "Urbach Tail Studies by Luminescence Filtering in Moderately Doped Bulk InP," *Applied Physics Letters* 97, no. 18 (2010): 181914, https://doi.org/10.1063/1.3510470.

81. K. Boubaker, "A Physical Explanation to the Controversial Urbach Tailing Universality," *The European Physical Journal Plus* 126, no. 1 (2011): 10, https://doi.org/10.1140/epjp/i2011-11010-4.

82. G. Gitonga Riungu, S. Waweru Mugo, J. Mbiyu Ngaruiya, G. Mbae John, and N. Mugambi, "Optical Band Energy, Urbach Energy and Associated Band Tails of Nano Crystalline TiO_2 Films at Different Annealing Rates," *American Journal of Nanosciences* 7, no. 1 (2021): 28, https://doi.org/10.11648/j.ajn.20210701.15.

83. S.-Y. Kim, T.-G. Lee, S.-A. Hwangbo, and J.-R. Jeong, "Effect of the TiO_2 Colloidal Size Distribution on the Degradation of Methylene Blue," *Nanomaterials* 13 (2023): 302, https://doi.org/10.3390/nano13020302.

84. J. F. Ramos-Justicia, A. Urbieta, and P. Fernández, "Refined Langmuir–Hinshelwood Kinetics for Heterogeneous Photocatalytic Systems: Analytical Closed-Form Solution, Enhanced Approximations and Experimental Validation," *Physchem* 6, no. 1 (2026): 5, https://doi.org/10.3390/physchem6010005.

85. N. O. Mainya, P. Tum, and T. M. Muthoka, "Photodegradation and Adsorption of Methyl Orange and Methylene Blue Dyes on TiO_2," *International Journal of Science and Research (IJSR)* 4 (2013): 3185–3189, https://www.ijsr.net/archive/v4i4/SUB153743.pdf, Access date: March 31, 2026.

86. R. Riedel, J. Schowarte, L. Semisch, et al., "Improving the Photocatalytic Degradation of EDTMP: Effect of Doped NPs (Na, Y, and K) Into the Lattice of Modified Au/TiO_2 Nano-Catalysts," *Chemical Engineering Journal* 506 (2025): 160109, https://doi.org/10.1016/j.cej.2025.160109.